Comparative Analysis of Numerical Schemes for Hypersonic Re-entry Flows

Bilal A. Bhutta* and Clark H. Lewis†
Virginia Polytechnic Institute and State University, Blacksburg, Virginia
and
Frederick A. Kautz II‡
Central Intelligence Agency, Washington, D.C.

Viscous and inviscid flowfields around a complex multiconic re-entry vehicle (with ablated nose shapes) are computed at three representative altitudes along a realistic re-entry trajectory. The effects of turbulence models on the aerodynamic predictions are studied. Results are presented for the trajectory and shape-change, inviscid flowfield, viscous shock-layer, and parabolized Navier-Stokes calculations. All the methods used in the study are discussed in terms of their accuracy in predicting the wall-measurable quantities and the aerodynamic forces and moments, the required computing times, solution efficiency and ease of application, and possible remedies for the most commonly encountered numerical difficulties. As a final note, the use of a viscous shock-layer scheme for the blunt-body solutions and the AFWAL parabolized Navier-Stokes scheme for the afterbody flowfield solutions are suggested as potential design and analysis tools for the range of re-entry conditions considered (30-150 kft).

Nomenclature

CA	= axial force coefficient
CM	= moment coefficient
CN	= normal force coefficient
L	= total vehicle length
M_∞	= freestream Mach number
MDOT	= surface mass-transfer ratio, $\rho_w v_w/\rho_\infty U_\infty$
p_∞	= freestream static pressure = PINF
P_{WALL}	= wall pressure
Q_{WALL}	= wall heat-transfer rate, Btu/ft^2/s
RB	= vehicle base radius
Re_∞	= freestream Reynolds number, 1/ft
RN	= unablated spherical nose radius
S	= surface streamwise distance
SMU	= explicit smoothing parameter in the AFWAL PNS code
SMUIM	= implicit smoothing parameter in the AFWAL PNS code
T_∞	= freestream static temperature, °R
U_∞	= freesteam velocity
v_w	= wall injection velocity
X	= axial body coordinate
XCG	= axial location of the center of gravity
XCP	= axial location of the center of pressure
α	= angle of attack, deg
θ	= cone half-angle, deg
γ	= flight path angle, deg
ψ	= local latitude, deg
λ	= local longitude, deg
ϵ_A, ϵ_B	= damping parameters in the AFWAL PNS code
ρ_∞	= freestream density

Subscript

w	= wall quantity
∞	= freestream quantity

Presented as Paper 83-1799 at the AIAA Applied Aerodynamics Conference, Danvers, Mass., July 13-15, 1983; received March 16, 1984; revision submitted July 26, 1984.

*Graduate Student, Aerospace and Ocean Engineering Department. Student Member AIAA.

†Professor, Aerospace and Ocean Engineering Department. Associate Fellow AIAA.

‡Engineer, Office of Scientific and Weapons Research. Member AIAA.

Introduction

OVER the past several years, the design and analysis of re-entry-type vehicles have become increasingly dependent upon numerical schemes for predicting the external flowfield. These numerical schemes have proven extremely useful in augmenting the experimental data base at various levels of analysis and design. Although the inviscid solution schemes remain as extremely useful tools, the development of bigger and better computational facilities has generated a significant amount of interest in accurate viscous methods. The various viscous solution schemes developed to date can be broadly classified as boundary-layer-type methods, viscous shock-layer (VSL) methods, parabolized Navier-Stokes (PNS) methods, and methods involving the time-dependent Navier-Stokes equations (e.g., the thin-layer Navier-Stokes schemes). Apart from providing more accurate data on the aerodynamic forces and moments, the viscous solutions have an added advantage of being able to provide estimates of the wall skin friction and wall heat-transfer rates. Both of these features are integral parts of the overall design and analysis of any re-entry vehicle.

The present study focuses mainly on the application and use of the available viscous and inviscid solution schemes. The inviscid analyses in this study were done with the NOL3D[1] and CM3DT[2] and 3IS[3] codes. The viscous blunt-body solutions for the ablated and unablated nose shapes were obtained with a three-dimensional viscous shock-layer method (VSL3D[4]). The viscous afterbody solutions were obtained using the three-dimensional viscous shock-layer scheme and two parabolized Navier-Stokes schemes. The PNS schemes used were an implicit noniterative scheme (AFWAL PNS code[5]) and an implicit iterative scheme (HYTAC PNS code[6]). The blunt-body solutions obtained by the VSL3D code were used to generate the initial data planes (IDPs) for the PNS solution schemes.

In this study we have attempted to present a complete aerodynamic analysis of a typical multiconic re-entry vehicle.

Starting from a coupled trajectory and shape-change analysis of the re-entry vehicle, complete flowfield analyses are done at various altitude points. The aim is to provide a potential user with enough guidelines to make similar calculations. Flowfield calculations are presented for a relatively complex flared-triconic re-entry vehicle. Although the actual shape change along the trajectory is a function of the vehicle geometry, in this study we have slightly simplified the analysis by considering the shape change of a relatively simpler sphere-cone vehicle with the same nose radius. This simplification is introduced because the shape-change code used in the present study (in its original form) cannot treat more complex vehicles than the "equivalent sphere-cones." A coupled trajectory and shape-change code (ASCC80[7]) was used to predict the shape change due to ablation, and the wall-temperature and surface mass-transfer distributions were obtained from a "quasi-steady-state" energy balance on the vehicle surface.[8]

One of the objectives of this study is to compare the predictions of various turbulence models under identical flight conditions. Three representative altitudes are considered along the chosen re-entry trajectory such that the flowfield conditions range from a fully laminar to an almost fully turbulent flow, and the nosetip ablation ranges from an unablated spherical nose to that of a severely ablated nose. The first altitude considered in this study is at 150 kft. At this altitude the nose is unablated, and the flow is strictly laminar. The second trajectory point considered is at approximately 50 kft and involves a slight nose shape change, with laminar flow over the nosetip and transition to turbulence occurring in the afterbody region. The lowest altitude considered is at 30 kft where severe nosetip ablation is encountered and transition to turbulence occurs in the nose region fairly close to the stagnation point. The turbulence models used in all of the three viscous codes are different and do not consider surface mass-transfer effects in the eddy-viscosity models. Although the turbulence models used in this study are strictly valid for no-surface-blowing conditions, the corresponding flowfield calculations did include the appropriate surface mass-transfer boundary conditions.

Solution Methods

The computational techniques used in the present study include a coupled trajectory and shape-change prediction method, methods for predicting surface mass-transfer and wall-temperature distributions, inviscid solution methods, and viscous solution schemes.

Shape-Change and Trajectory Calculations

The ASCC80 code (ABRES Shape Change Code-1980[7]) was used to predict the nosetip shape change for an initial sphere-cone vehicle. The current version of the shape change code possesses a three-degree-of-freedom trajectory modeling capability which enables the prediction of re-entry trajectories while accounting for the effects of nosetip shape change.

In the ASCC80 code, a boundary-layer solution is performed over the nosetip using a momentum-energy-integral technique. The surface pressure distribution is computed from semiempirical relations, and the wall conditions to be used in the boundary-layer solutions are determined from a surface energy balance. The influence of various effects such as surface curature, transpiration, particle-flowfield interactions, and transition are included through the use of influence coefficients. The results of the ASCC80 computations provide the ablated nose shapes in terms of discreet spatial coordinates. These coordinates are then fit with piecewise-analytic curves using the QUICK geometry package developed by Vachris and Yaeger.[9]

Surface Mass-Transfer and Wall-Temperature Distributions

The surface mass-transfer and wall-temperature effects are important features of high speed viscous flows. In the present study, these distributions are determined by an iterative solution of the steady-state surface-energy-balance equations.[8] These energy-balance equations are closed through the use of correlations based on a combination of experimental and theoretical results. Presently this scheme includes six of the most common surface materials used for re-entry-type applications; namely, graphite, carbon-phenolic, Teflon, silica-phenolic, quartz-phenolic, and asbestos-phenolic materials.

Inviscid Solutions

The inviscid solutions for the cases where the nosetip remained unablated and spherically blunted were computed using the NOL3D code. This code is based on the inverse method of Lomax and Inouye[10] for computing the subsonic/transonic flowfield over a spherical nosetip. The initial data plane for the afterbody solution is obtained by a method of characteristics rotation to axis-normal coordinates. For the inviscid afterbody solution the NOL3D code uses the conservation form of the inviscid steady-flow equations. Second-order finite-difference approximations are used to obtain the numerical solution.

The inviscid solution for re-entry vehicles with ablated nosetips involves a considerably more difficult and involved approach. The time-dependent CM3DT[2] method was used for predicting the subsonic/transonic flowfields over such nonspherical nosetips. This method uses the unsteady Euler equations to obtain the steady-state solution as the time-asymptotic limit. These solutions were used to provide initial data for the 3IS inviscid supersonic flowfield code.[3] In 3IS, a spatially marching finite-difference technique is used to solve the nonconservation form of the inviscid equations. The CM3DT solution scheme uses a body-normal coordinate system, whereas the 3IS solution scheme uses an axis-normal coordinate system.

Viscous Shock-Layer Solutions

The three-dimensional viscous shock-layer equations are derived from the full Navier-Stokes equations by first scaling with respect to variables which are of order one in the near-wall region, and then by scaling with respect to variables which are of order one near the shock. Such a scaling results in equations which are uniformly valid from the wall to the shock. In this way the problems associated with the coupling of the outer-inviscid and the inner-viscous region (typical of the boundary-layer-type methods) are eliminated. Also, in this approach the higher-order boundary-layer effects such as the displacement-thickness effects, effects of vorticity interaction, and the effects of longitudinal and transverse curvature are consistently treated.

For a fairly complete picture of the various developments, updates, and numerical tests with the VSL solution scheme the

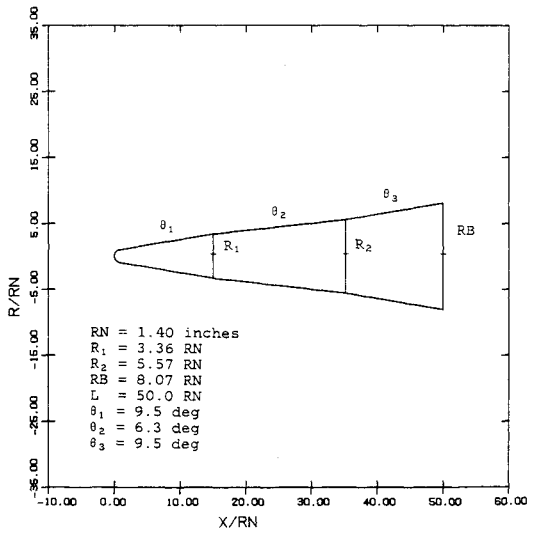

Fig. 1 Unablated re-entry vehicle geometry.

reader is referred to Murray and Lewis.[4] However, briefly speaking, the three-dimensional viscous shock-layer solution begins in the nose region by first obtaining an axisymmetric stagnation point solution in a wind-fixed coordinate system, which is subsequently rotated to generate the initial profiles for the three-dimensional afterbody flowfield solution. At a given streamwise station the three-dimensional solution begins from the windward plane and marches around the body to obtain a converged solution at each circumferential location. In case of crossflow separation, the circumferential marching is stopped, and from that streamwise location onwards, these circumferential planes are not computed. For turbulent flowfield calculations, the present VSL3D scheme uses the two-layer eddy-viscosity model of Cebeci and Smith.[11]

Recently, Thompson et al.[12] successfully used the VSL3D scheme to predict the flowfields over a series of ablated nosetips under various flow conditions. These results clearly show that the VSL3D blunt-body solutions are not only comparable in quality to the TLNS blunt-body solutions but also require computing times which are only a small fraction of the TLNS computing times.

HYTAC PNS Solution

The governing equations in the HYTAC PNS code[6] are based on the steady parabolized Navier-Stokes equations written in a body-normal and shock-normal coordinate system. These equations are parabolic in the streamwise direction and elliptic in the crossflow direction. These equations are solved by an implicit differencing in the crossflow direction and a two-point backward differencing scheme in the streamwise direction. The required crossflow and surface-normal derivatives are obtained using an unequally spaced three-point differencing formula.

The aforementioned difference equations are linearized by a Newton-Raphson scheme, and all nonlinear terms involving the perturbation quantities are ignored. In view of the large system of equations to be solved, a Gauss-Seidel iteration procedure is employed instead of a direct solution scheme. At present, the entire regime of laminar, transitional, and turbulent flows can be treated in the HYTAC code. The two-layer eddy-viscosity model of Hung and MacCormack[13] is used to model the turbulent flows.

Previously the HYTAC PNS code was modified by Kim et al.[14] and Kim and Lewis[15] to include surface mass-transfer, variable wall temperature, spin and yaw capabilities.

AFWAL PNS Solution

The AFWAL PNS code[5] is based on the Schiff-Steger method[16] of solving the conservation equations and involves an axis-normal coordinate system. The formulation involves a "viscous-sublayer approximation" in which a constant pressure is imposed in the subsonic part of the viscous region, and this is essential for maintaining non-negative eigenvalues near the wall.[14] Further stability is provided by adding fourth-order dissipative terms to the governing equations. The resulting equations are linearized and cast into a delta form. At each marching step the outer bow shock is propagated using an explicit shock prediction scheme.[5] The turbulence model used is the Baldwin-Lomax model,[17] which is patterned after the Cebeci-Smith model.[11] Such a model avoids the requirement of determining the boundary-layer edge. The final system of equations is solved using an approximate factorization algorithm which reduces the overall inversion process into a sequence of implicit inversions involving only tridiagonal systems.

We have recently updated the AFWAL PNS code to include a piecewise-continuous geometry. The input is provided in terms of the QUICK geometry package developed by Vachris and Yaeger.[9] We have also modified the original AFWAL PNS code to include a variable step-size distribution, a variable wall-temperature distribution, and surface mass-transfer effects. The use of a variable step-size distribution significantly reduced the required computing time. Earlier studies[12] have shown that under turbulent flow conditions, the use of two-point and four-point difference formulas may produce marked differences in the predicted wall-measurable quantities. In view of this observation, in the present study the wall-measurable quantities (such as heat-transfer rates and skin friction) have been computed using four-point differencing formulas.

Results and Discussion

Complete flowfield solutions were obtained at three representative altitudes along a typical re-entry trajectory. The three trajectory points chosen to perform complete flowfield solutions were at the altitudes of approximately 150, 50, and 30 kft. In this paper these altitude cases are referred to as Cases A, B, and C, respectively. The calculations for Cases A and B were done for zero and 2-deg angles of attack, whereas Case C calculations were only done for a zero angle-of-attack condition. The freestream conditions for each of these cases are given in Table 1. The unablated shape of the re-entry vehicle used in this study is shown in Fig. 1. This flared-triconic vehicle has a front cone half-angle of 9.5 deg. The triconic afterbody consists of a 3.2-deg expansion corner followed by a 3.2-deg compression corner. The vehicle has an initial nose radius of 1.4 in. and an axial length of 50 nose radii. All lengths have been nondimensionalized with the nose radius.

The nosetip geometries (as predicted by ASCC80 code) at the three altitudes being considered as shown in Fig. 2. The nosetip profiles shown in this figure are the analytic curve-fits of the actual ASCC80 nose-shape data and have been obtained using the QUICK geometry description package.[13] For Case A, the nosetip is unablated and remains spherical.

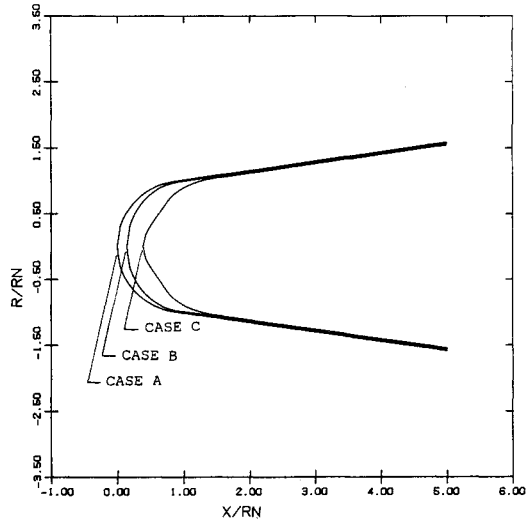

Fig. 2 Ablated nose shapes for Cases A, B, and C.

Table 1 Freestream conditions

	Case A	Case B	Case C
Alt, ft	150,000	50,249	30,171
M_∞	22.26	22.63	19.00
U_∞, ft/s	23803	21878	18907
T_∞, °R	476.15	388.99	412.06
p_∞, psf	2.8445	241.9600	618.8137
ρ_∞, slug/ft^3	3.4813$E-5$	3.6249$E-3$	8.7529$E-4$
Re_∞, 1/ft	2.3707$E+4$	2.6758$E+5$	5.3223$E+7$
Flow Type			
nose:	Laminar	Laminar	Lam/Trans
body:	Laminar	Trans/Turb	Turbulent
S/RN trans.	–	3.7430	0.2174

For Case B, the transition to turbulence occurs downstream on the conical afterbody, and the nose shape is elliptical. Case C has transition to turbulence occurring in the nosetip region resulting in a small elliptically shaped region around the stagnation point, and the remaining nose shape is almost conical. For all the turbulent cases considered herein, the transition from laminar to turbulent flow conditions was initiated instantaneously. The VSL full-body results were done for comparison purposes only and thus only the zero angle-of-attack cases were considered in obtaining them.

Trajectory and Shape-Change Calculations

The initial conditions for the ASCC80 shape-change calculations are listed in Table 2. As mentioned earlier these calculations were carried out on a sphere-cone vehicle with the same nose radius, axial length, weight and base radius as the flared-triconic vehicle being considered herein.

The nose shapes and the freestream conditions for the three altitudes were used to obtain the inviscid surface-pressure distributions by either the NOL3D or the CM3DT and 3IS codes. The inviscid pressure distributions over the entire body (along with the information on surface material and the location of transition to turbulence) were used to predict the surface mass-transfer and wall-temperature distributions. For the present study, the nose material was taken as carbon-carbon, whereas the afterbody was taken to be made of a carbon-phenolic material. The carbon nose was assumed to be 3.5 nose radii long. The wall-temperature and surface mass-transfer distributions for Case B are shown in Fig. 3. The results show that the expansion and/or compression corners can produce sizeable differences in the surface mass-transfer and wall-temperature distributions. Expansion corners tend to decrease these values, whereas the compression corners increase them. Surface material discontinuities, however, produce a different trend. On changing from carbon to a carbon-phenolic material the mass-transfer rates almost double; however, the wall cools down and the surface temperature drops. The effect of turbulence is generally to increase the wall temperature and the surface mass-transfer rates. The wall-temperature and surface mass-transfer distributions obtained for Case A and Case C conditions were qualitatively similar to the predictions for Case B.

Table 2 Initial conditions for trajectory calculations

	Shape-change
Altitude, ft	200,404
U_∞, ft/s	23758
γ, deg	−26.24
ψ, deg	0.0
λ, deg	0.0

Table 3 Axial force data for $\alpha = 0$ deg

Code	Case A	Case B	Case C
NOL3D	0.046939	–	–
CM3DT+3IS	–	0.047592	0.049089
VSL3D	0.056933	0.051052	0.048792
VSL/AFWAL	0.061051	0.054951	0.056802
VSL/HYTAC	0.060300	0.059925	0.061602

Inviscid Solutions

The inviscid flowfield calculations were done using either the NOL3D code or the CM3DT and 3IS codes. Since the NOL3D code is restricted to spherical nose shapes, it was only used for the Case A calculations. Due to the nonspherical nose shapes for Cases B and C, these calculations were done using the CM3DT and 3IS codes.

The zero and nonzero angle-of-attack results of the NOL3D code for the Case A conditions are shown in Figs. 4 and 6. These results show that although there is good agreement of the surface pressures on the windward side, the inviscid solution underpredicts the leeward pressures by nearly 20%. Tables 3 and 4 show the comparisons of the corresponding force and moment predictions. These results show that despite good agreement of the wall-pressure distributions, the inviscid axial-force estimates are considerably lower. These differences are a direct consequence of the viscous effects.

The CM3DT and 3IS results for Cases B and C are shown in Figs. 4 and 8. Figure 4 is for the conditions of Cases B and C at a zero angle of attack, whereas Fig. 8 is for Case B at a 2-deg angle of attack. The 3IS code uses an axis-normal coordinate system, which causes difficulties in starting the solution in regions of large body curvatures. The remedy for such starting problems is to start the solution as far downstream as the CM3DT solution will permit. Usually the quality of the CM3DT solution is degraded by extending the solution too far downstream; thus, a judicious choice of the starting location is important for preventing numerical difficulties and inaccuracies. The force and moment comparisons for these results are given in Tables 3 and 4. These results show that (similar to the Case A results) the inviscid results for Cases B and C substantially underpredict the aerodynamic forces and moments.

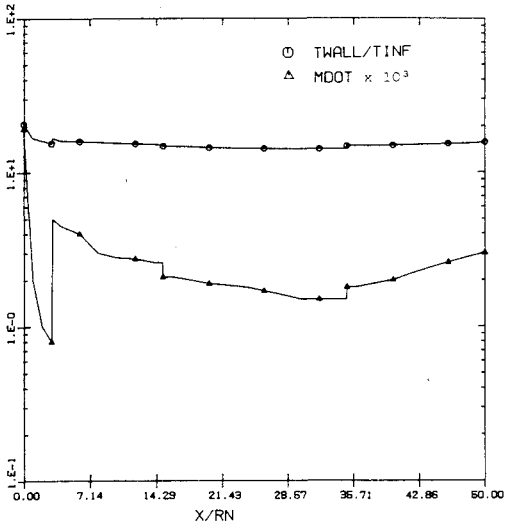

Fig. 3 Surface mass-transfer and wall-temperature distribution for Case B.

Table 4 Force and moment data for $\alpha = 2$ deg

Case	Code	*CA*	*CN*	*CM*	*XCP/L*
Case A	NOL3D	0.051175	0.070537	−0.054402	0.77127
	VSL/AFWAL	0.064457	0.071080	−0.053325	0.75018
	VSL/HYTAC	0.071014	0.075260	−0.059370	0.78887
Case B	CM3DT+3IS	0.051860	0.071220	−0.055450	0.77860
	VSL/AFWAL	0.058666	0.073432	−0.055217	0.75195
	VSL/HYTAC	0.065098	0.064989	−0.050440	0.77619

Viscous Solutions

The results of the viscous calculations for Cases A, B, and C are given in Figs. 4-9. Figures 4 and 6 show the wall-pressure distributions for Case A; whereas, Figs. 5 and 7 show the corresponding distributions of the wall heat-transfer rates. These results show good agreement between the viscous predictions, especially between the two PNS (HYTAC and AFWAL) calculations, which are in excellent agreement with each other. It should be noted that the quality of the VSL solution depends on the accuracy of the input shock shape. Furthermore, due to the parabolic nature of the VSL equations any errors at the junctures will be propagated a short distance downstream, even if the input shock is of a good quality. This may be the reason for the observed inaccuracies in the VSL results over the flared afterbody. The HYTAC PNS calculations for this case were made using nine circumferential planes and 50 body-normal grid points. The AFWAL PNS calculations used 17 circumferential planes and 30 axis-normal grid points, and the VSL blunt-body solutions for the angle-of-attack cases were made using nine circumferential planes and 101 body-normal grid points. With these grids, no problems were encountered in starting the PNS afterbody solutions for Case A at zero and nonzero angles of attack.

The results for Case B are shown in Figs. 4, 5, 8, and 9. At this altitude the afterbody flow is fully turbulent, and the wall quantities show a significant variation from one code to another. It is to be noted that the turbulence models used in each of the viscous codes are different and do not include mass-transfer effects in the eddy-viscosity models. These results show that the Cebeci-Smith model used in VSL3D agrees better with the Baldwin-Lomax model used in the AFWAL PNS code. The predictions of HYTAC PNS code are based on the Hung and MacCormack model and differ from the other models by an order of magnitude. This is in contrast to our earlier experiences,[12] where the Hung-MacCormack model agreed better with the Cebeci-Smith model, and the Baldwin-Lomax model differed by an order of magnitude. These results indicate that none of the available turbulence models are equally dependable under all conditions. Thus, it would be unwise to pick a particular model and be fully confident of the predictions under all conditions. At crucial stages of any analysis it becomes increasingly important to have more than one turbulence modeling capability in order to cross-check the predictions. This is more of a limitation due to the state-of-the-art in turbulent flowfield analyses than a deficiency in any one of the numerical prediction schemes.

As the flow in the nose region for Case B is laminar, no numerical difficulties were encountered in starting the PNS afterbody solutions. However, in the HYTAC PNS code severe numerical difficulties were encountered in the downstream region. The problem was traced to the number of body-normal grid points being used, and solutions became possible when the total number of such grid points was increased from 50 to 101. Furthermore, due to the body-normal and shock-normal coordinate system used in the HYTAC PNS code, it became necessary to start the afterbody solution downstream of the tangent point and not use very small separations between the four IDP locations in order to avoid regions of large body- and shock-curvatures. An IDP separation distance of 0.06-0.05 nose radii was found to be generally adequate.

The results for Case C are shown in Figs. 4 and 5. The flow conditions for this case are almost fully turbulent, except for a very small region around the stagnation point. These results are only for a zero angle-of-attack condition because severe numerical difficulties were encountered for the angle-of-attack conditions. The reason for these numerical problems can be better understood from the zero angle-of-attack results. Figure 5 shows the wall heat-transfer rates for this case. Examining this figure, one can see a significant discontinuity in the wall heat-transfer rates at the IDP location. This observation is consistent with the Case B results and is due to the differences between the turbulence models used in the afterbody and the nose regions. Although under zero angle-of-attack

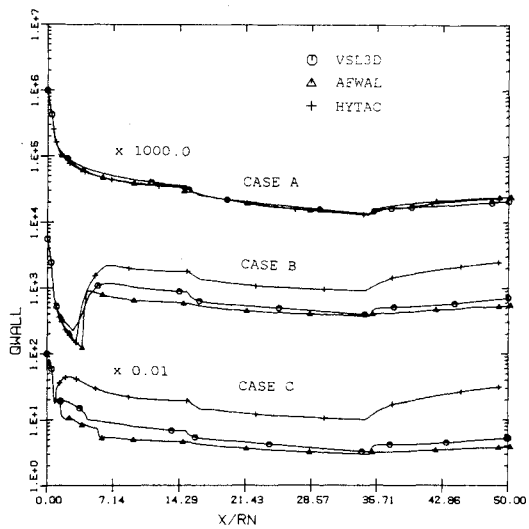

Fig. 5 Wall heat-transfer rates for Cases A, B, and C at $\alpha = 0$ deg.

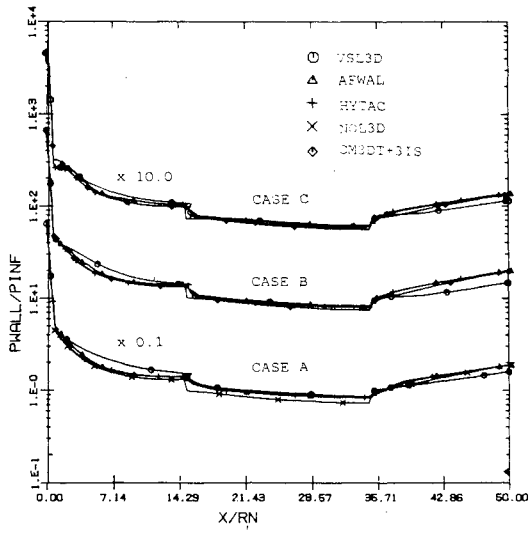

Fig. 4 Surface pressure distributions for Cases A, B, and C at $\alpha = 0$ deg.

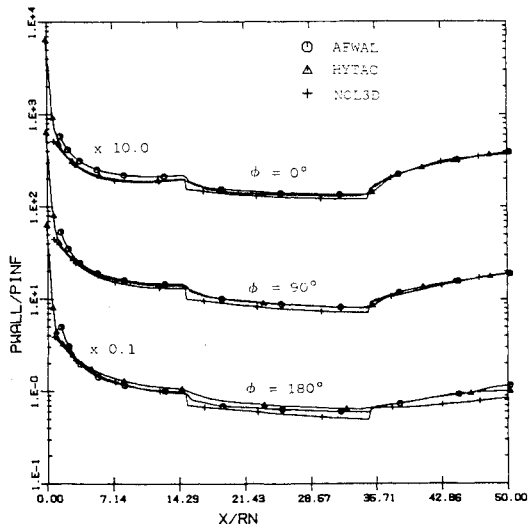

Fig. 6 Surface pressure distribution for Case A at $\alpha = 2$ deg.

conditions the mismatch is significant, it was still possible to obtain the PNS afterbody solutions. A nonzero angle of attack considerably amplified this mismatch on the leeward side, and the inconsistency between the starting solution and the afterbody solution scheme was strong enough to prevent the afterbody solution from starting at all. These results clearly suggest that in order to prevent any inconsistency with the starting solution, the afterbody solutions for fully turbulent flow conditions should be started from a blunt-body solution which uses the same (or reasonably similar) turbulence model.

Comments on the AFWAL PNS Solutions

The AFWAL PNS solutions are heavily dependent upon the various smoothing and step-size parameters which are user-supplied information. The choice of these parameters is a matter of great significance. A small scale sensitivity study is essential before embarking upon the final calculations. From our experience we have found that a normal step size of 0.08% of the local shock-layer thickness is an adequate choice. For the streamwise step size, we recommend the use of a step size of 0.02-0.03 nose radii in the nose region and 0.5-1.0 nose radii in the afterbody region. The explicit and implicit smoothing parameters (SMU and SMUIM)[5] do not have a significant impact on the solution, and we have found the values of SMU = 0.2 and SMUIM = 0.6 to be appropriate. The damping parameters ϵ_A and ϵ_B,[5] on the other hand, have a strong effect on the solution accuracy and should have the smallest value possible for maintaining stable and smooth results. The values of $\epsilon_A = \epsilon_B = 0.1$-0.3 are appropriate as a starting estimate.

It should be mentioned that although the present calculations with the AFWAL PNS code did not pose any significant problems, we have experienced a great deal of difficulty in obtaining solutions for high altitude cases (200 kft and above). Under these conditions, the major problem was observed to be the near-wall region where the solution became unstable.

Computing Times

The representative computing times for the test cases considered in this study are shown in Table 5. In considering the Case C computing times, it should be noted that AFWAL PNS solution for these zero angle-of-attack conditions were also obtained with 17 circumferential planes because the present AFWAL PNS code lacks an axisymmetric solution capability. The corresponding HYTAC PNS solutions are for three circumferential planes; whereas, the VSL3D solutions are one-plane axisymmetric calculations. The VSL3D full-body calculations were not made for the angle-of-attack cases and thus are not included in these comparisons.

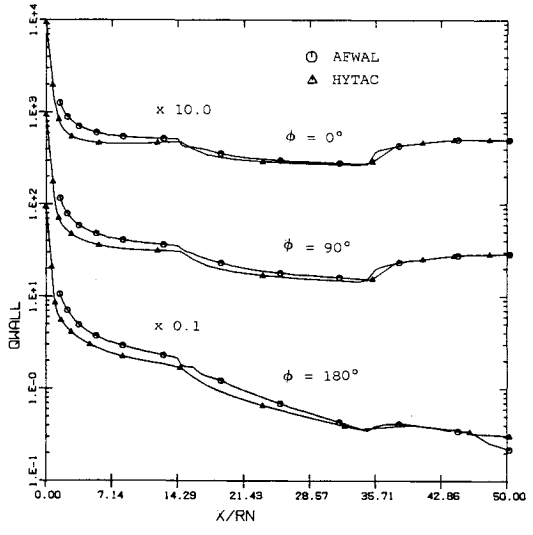

Fig. 7 Wall heat-transfer rates for Case A at $\alpha = 2$ deg.

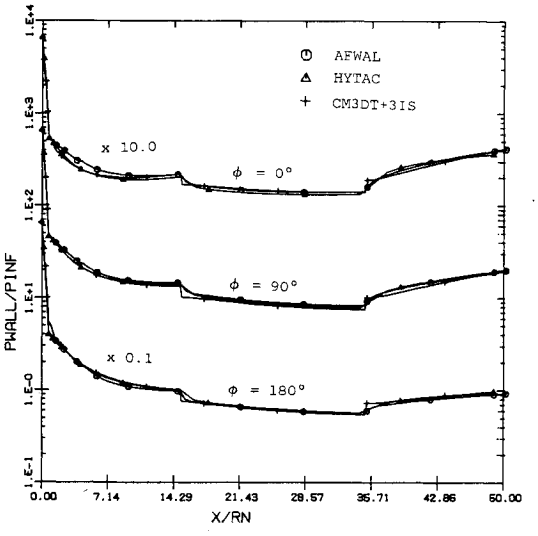

Fig. 8 Surface pressure distribution for Case B at $\alpha = 2$ deg.

Table 5 Computing times[a]

Case	Case	$\alpha = 0$ deg t, min:sec	$\alpha = 2$ deg t, min:sec
Case A	NOL3D	0:19	0.32
	VSL3D	0:53	–
	VSL/AFWAL	11:00	14:47
	VSL/HYTAC	1:52	7:47
Case B	CM3DT + 3IS	17:28	17:35
	VSL3D	1:80	–
	VSL/AFWAL	10:20	14:19
	VSL/HYTAC	5:02	19:14
Case C	CM3DT + 3IS	17:18	–
	VSL3D	1:90	–
	VSL/AFWAL	10:27	–
	VSL/HYTAC	6:19	–

[a]CPU time on IBM 370/3081 with H-compiler and OPT2 optimization.

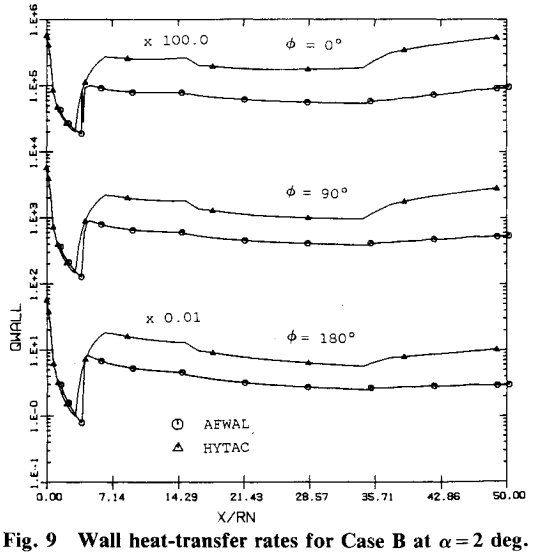

Fig. 9 Wall heat-transfer rates for Case B at $\alpha = 2$ deg.

Conclusions

In the present study, numerical predictions of the flowfields over a complex multiconic re-entry vehicle (with ablated nose shapes) are presented at three representative locations along a typical re-entry trajectory. Predictions of various inviscid and viscous codes are compared in terms of the wall-measurable quantities, the aerodynamic forces and moments, and the computational efficiency. The question of suggesting a numerical scheme for the design and analyses of re-entry vehicles is addressed, and possible solution strategies are discussed. Based on the results of this study, the following conclusions have been drawn:

1) The inviscid codes are useful tools for obtaining initial estimates of the aerodynamic forces and moments. However, these estimates may be significantly different from the viscous predictions.

2) The computational accuracy and efficiency of the VSL blunt-body solutions are fully adequate for providing the starting solutions for the PNS afterbody flowfield solution schemes.

3) In order to prevent numerical difficulties in starting the PNS afterbody flowfield solutions, the turbulence model used in the afterbody region should be reasonably close to (if not the same as) the one used to obtain the turbulent blunt-body solution. Furthermore, as the available data on turbulent flows lack in being able to indicate the best turbulence model under a given set of flow conditions, multiple turbulence modeling capabilities in a code are essential.

4) The results indicate that at present a full-body solution capability based on a VSL3D blunt-body solution and an AFWAL PNS afterbody flowfield solution is the most appropriate tool for design and analysis purposes.

Appendix

This section includes the piecewise-analytic description of the ablated nose shapes used in this study. For Case A, the nose was spherical with a nose radius of 1.4 in. All dimensions have been nondimensionalized with respect to a nose radius, and the origin of the coordinate system is at the nose tip.

Case B

$0 \le x \le 0.77107$	$ax + bx^2 + y^2 = 0$
	$a = -2.21099,\ b = 1.25014$
$0.77107 \le x \le 50.0$	$ax + by = 0$
	$a = 7.09098,\ b = -49.22893$

Case C

$0 \le x \le 0.36664$	$ax + bx^2 + y^2 = 0$
	$a = -0.73809,\ b = -1.01021$
$0.36664 \le x \le 1.08935$	$ax + by + cx^2 + y^2 = 0$
	$a = -0.57426,\ b = 0.39317$
	$c = 0.28771$
$1.08935 \le x \le 50.0$	$ax + by = 0$
	$a = 7.03255,\ b = -48.9107$

References

[1]Solomon, J.M., Ciment, M., Ferguson, R.E., Bell, J.B., and Wardlaw, A.B. Jr., "A Program for Computing Steady Inviscid Three-Dimensional Supersonic Flow on Reentry Vehicles, Vol. 1, Analysis and Programming," Naval Surface Weapons Center, White Oak Laboratory, Silver Spring, Md., NSWC/WOL/TR 77-28, Feb. 1977.

[2]Hall, D.W. and Dougherty, C.M., "Performance Technology Program (PTP-S II), Vol. III—Inviscid Aerodynamic Predictions for Ballistic Reentry Vehicles with Ablated Nosetips," Ballistic Missile Office, Norton AFB, Calif., BMO TR, Sept. 1979.

[3]Daywitt, J., Brant, D. and Bosworth, F., "Computational Technique for Three-Dimensional Inviscid Flow Fields about Reentry Vehicles, Volume I—Numerical Analysis," Air Force Space and Missile Systems Organization, Los Angeles, Calif., SAMSO TR-79-5, April 1978.

[4]Murray, A.L. and Lewis, C.H., "Hypersonic Three-Dimensional Viscous Shock-Layer Flows over Blunt Bodies," *AIAA Journal,* Vol. 16, Dec. 1978, pp. 1279-1286.

[5]Shanks, S.P., Srinivasan, G.R., and Nicolet, W.E., "AFWAL Parabolized Navier-Stokes Code: Formulation and User's Manual," Air Force Flight Dynamics Laboatory, Wright-Patterson AFB, Ohio, AFWAL-TR-82-3034, June 1982.

[6]Helliwell, W.S., Dickinson, R.P., and Lubard, S.C., "HYTAC Phase I Report, Viscous Flow over Arbitrary Geometries at High Angle of Attack," Arete Associates, Encino, Calif., Tech. Rept. AR-79-046-TR, April 1979.

[7]Murray, A.L. and Saperstein, J.L., "User's Manual for the Updated ABRES Shape Change Code (ASCC80)," Reentry Vehicle Technology Program Final Report, Vol. 3, Pt. 1, Mountain View, Calif., Acurex Rept. FR-80-38/AS, Oct. 1980.

[8]Thompson, R.A., "Viscous Shock-Layer Flows over Multiconic Reentry Vehicles," M.S. Thesis, Virginia Polytechnic Institute and State University, Blacksburg, Va., May 1983.

[9]Vachris, A. and Yaeger, L., "QUICK-GEOMETRY, A Rapid Model for Mathematically Modeling Configuration Geometry," NASA SP-390, 1975.

[10]Lomax, H. and Inouye, M., "Numerical Analysis of Flow Properties about Blunt Bodies Moving at Supersonic Speeds in an Equilibrium Gas," NASA TR R-204, July 1964.

[11]Cebeci, T., "Behavior of Turbulent Flows near a Porous Wall with Pressure Gradient," *AIAA Journal,* Vol. 8, Dec. 1970, pp. 2152-2156.

[12]Thompson, R.A., Lewis, C.H. and Kautz, F.A., II, "Comparison of Techniques for Predicting 3-D Viscous Flows Over Ablated Shapes," AIAA Paper 83-0345, Jan. 1983.

[13]Hung, C.M. and MacCormack, R.W., "Numerical Solution of Three-Dimensional Shock Wave and Turbulent Boundary-Layer Interaction," *AIAA Journal,* Vol. 16, Oct. 1978, pp. 1090-1096.

[14]Kim, M.D., Thareja, R.R., and Lewis, C.H., "Three-Dimensional Viscous Flowfield Computations in a Streamline Coordinate System," *Journal of Spacecraft and Rockets,* Vol. 1, Jan.-Feb. 1982, pp. 41-45.

[15]Kim, M.D. and Lewis, C.H., "Computations of Hypersonic Viscous Flows over a Body with Mass Transfer and/or Spin," *Journal of Spacecraft and Rockets,* Vol. 20, March-April 1983, pp. 101-107.

[16]Schiff, L.B. and Steger, J.L., "Numerical Simulation of Steady Supersonic Viscous Flow," AIAA Paper 79-0130, Jan. 1979.

[17]Baldwin, B.S. and Lomax, H., "Thin Layer Approximation and Algebraic Model for Separated Turbulent Flows," AIAA Paper 78-0257.